Materials Today Communications 35 (2023) 106059

Contents lists available at ScienceDirect

Materials Today Communications

journal homepage: www.elsevier.com/locate/mtcomm

A model for damage and failure of carbon-carbon composites: development and identification through Gaussian process regression

Alessandro Airoldi [a], Edoardo Novembre [a,*], Chiara Mirani [a], Giacomo Gianotti [a], Raffaello Passoni [b], Carlo Cantoni [b]

[a] Dept. of Aerospace Science and Technology, Politecnico di Milano, Via La Masa 34, 20156 Milano, Italy
[b] Brembo S.p.A., Curno, BG, Italy

ARTICLE INFO

Keywords:
2.5D carbon-carbon
Composite damage model
Genetic algorithm
Gaussian process regression

ABSTRACT

The paper presents a model for damage accumulation and failure of carbon-carbon (C/C) thick laminates used in automotive disc brakes, with 2.5D reinforcement and disordered lamination sequences. The highly non-linear response of laminates in different stress states was acquired through tensile and Double Cantilever Beam tests performed on specimens cut from discs. The paper adopts a novel bi-phasic approach based on Cohesive Zone Model to model delamination, matrix cracking and fibres failure to predict the structural integrity of laminates. Since the non-homogeneous lay-ups required a robust identification tool for the material properties, modern automatic techniques were used, such as genetic optimization and non-parametric Gaussian process regression, to identify the material model parameters both in the elastic and inelastic ranges. Considering all the tests, the qualitive and quantitative correlation that was achieved indicates that the constitutive law adopted adequately represents the physical damage mechanisms of the C/C material in severe load conditions and that the identification methods adopted represent effective tools to calibrate complex material models for the prediction of the strength and damage tolerance of C/C and, in general, composite laminates.

1. Introduction

Carbon-carbon composites (C/C) are a class of advanced materials consisting in carbon fibres embedded in a graphitic matrix, which result from the densification of a carbon-fibre preform with a vapour- or liquid-phase carbon precursor. Although their properties highly depend on the manufacturing process, as typical in composites, they are generally characterized by remarkable strength and stiffness at high temperature ($T > 2500\,^{\circ}C$), high thermal conductivity, low coefficient of thermal expansion [1], relevant energy absorption capability, high fracture toughness [2] and excellent frictional properties [3]. For these reasons, they are primarily employed in high temperature applications, such as aeronautical brakes or thermal protection systems for re-entry vehicles, being ablatives or hot structures [4–6].

The architecture of the fibrous preform influences both the mechanical performances and the cost of the material [7]. A popular and relatively inexpensive manufacturing process to produce preforms is needling, which was introduced in the 80 s by SEP (now Snecma Propulsion Solide) with the family of 3D materials called Novoltex [8–10]. The preform of Novoltex is made by an alternation of fabrics and layers of short fibres. The needling phase consists in attaching fabrics to each other by transferring some of the short fibres in the through-the-thickness direction with hooks-fitted needles [9]. For their thermo-mechanical properties, these materials were selected for manufacturing engine nozzles and aircraft brakes [8,10]. The needling procedure is also employed to produce 2.5D C/C laminates by replacing fabrics with UD layers. Since they offer good compromise between mechanical performances and manufacturing cost, 2.5D C/C and Ceramic Matrix Composites (CMCs) have been extensively investigated [11–14].

As already mentioned, C/C have been selected for the first time for braking systems by the aerospace industry because they offered an extraordinary weight saving compared to steel (between 40 % and 60 %), better heat capacity, and increased service life [4,15]. For the same reasons, C/C brakes are nowadays the standard in Formula 1 race cars [16] where the needling technology, combined with chemical vapour infiltration (CVI), is employed to produce 2.5D C/C braking discs. This application requires complex geometries with holes, notches and

* Corresponding author.
E-mail address: edoardo.novembre@polimi.it (E. Novembre).

https://doi.org/10.1016/j.mtcomm.2023.106059
Received 15 February 2023; Received in revised form 11 April 2023; Accepted 22 April 2023
Available online 25 April 2023

structural details that are obtained by machining a rough disc. Such geometrical features, the action of the brake pads and the mechanical constraints lead to complex thermomechanical loading conditions and significant stress concentrations. Moreover, C/C are characterized by a pseudo-plastic behaviour, by multiple and gradual damage mechanisms and by a "graceful failure" [17]. As a consequence, the experience gained in disc design indicates that a purely elastic strength analysis provides very conservative results.

The numerical modelling of C/C has often been addressed via multiscale or FE micromechanical approaches, for the purpose of investigating how the architecture, porosity, and microstructure of the material impact its properties [18–21]. However, the previous considerations suggest that reliable analyses for structural integrity, and the possible application of a damage tolerant approach, demand the modelling of the mechanical behaviour of the whole structural component beyond the elastic range. Furthermore, as demonstrated by the experimental investigation proposed in [22], the damage tolerance behaviour of C/C laminates with UD reinforcement is characterized by extremely complex damage scenarios, which involve both fibres and matrix, and therefore the model of the material being studied should be able to represent both fibres damage and matrix fractures. Such aspects drive toward finite element approaches developed at the mesoscale level.

In the aforementioned context, the bi-phasic approach proposed in [23] for polymeric matrix composites could represent an effective solution. In this approach, the material was decomposed in a fibre phase and a matrix phase, which were characterized by constitutive responses formulated as a function of the same average strain state in the ply. Although the phases were idealized and the approach has not to be considered a true micromechanical model, the decomposition gave the opportunity to define separate constitutive responses that represented matrix-dominated or fibre-dominated inelastic processes. Such possibility was exploited, in the case of polymer matrix composites, in bi-phasic models that have been employed to represent complex damage scenarios in crashworthiness applications [24,25].

Considering CMC laminates, in [26] the binary model described in [27,28] was successfully applied and exploited to represent the non-linear response in the plane of the laminae. A mesh of solid elements and a plasticity model associated to Drucker-Prager yield criterion were used to represent the non-linear response of an effective medium representing the matrix phase, while, on the other hand, one-dimensional elements were used to represent the stiffness contribution of the continuous fibres in the reinforcement directions.

However, another fundamental damage mechanism that must be considered in composite laminates is delamination. In modern mesoscale approaches, a ply-wise modelling technique is conventionally applied, and delamination is frequently modelled by using CZM in layers of zero- or infinitesimal-thickness cohesive elements located between the elements representing the separate plies [29,30]. Other methods to model material interfaces and crack propagations are available, for instance [31,32]. Exploiting the techniques that were presented and validated in [33–37], the method proposed in [23] combines the embedment of a CZM in finite-thickness elements with a bi-phasic approach. This eliminates the need of zero-thickness interface elements, which are known to require a careful calibration and to cause numerical problems or inefficiencies [38,39], and makes possible a description of both intralaminar damage and delamination within a single constitutive law, thus allowing the introduction of coupling between the two types of damage.

In this work, the approach described in [23] was applied with slight modifications to model the inelastic response of the 2.5D C/C under study, both considering in-plane damage and delamination. The development of the approach had to face a significant issue, since the calibration and the validation of the material properties were complicated by the peculiar lay-up of the C/C laminates in the brake discs. This issue stems from the sophistication of the manufacturing process of the C/C preforms, which involves the production of laminates with odd and disordered lamination sequences that continuously vary in the volume of the disc.

A viable solution for the identification of both elastic constants and damage laws parameters was found by using specimens directly cut from CVI-produced discs with partially controlled lay-ups, and by resorting to regression models and genetic algorithms. The choice of resorting to partially controlled lamination sequences was dictated by the difficulty to obtain preforms with completely homogeneous lay-ups, which are typically adopted in composite lamina characterization. It is also worth noting that the manufacturing process required to obtain a homogeneous preform could lead to different material porosity and defects after the CVI densification, and ultimately to specimens with different response with respect to the actual laminates.

Example of adoption of numerical approaches for the automatic identification of material parameters can be found in [40,41] for the elastic constants of composites, in [42] for the interfacial parameters of composites, and in [43] for the damage parameters of the Gurson's plasticity model. In the work presented in this paper, the genetic algorithm was directly applied for the identification of elastic parameters, while the computational cost involved in non-linear analyses suggested to use an approach based on meta-modelling, built up by adopting a Gaussian Process Regression method, for the parameters that define the inelastic behaviour of the material.

The present paper is therefore organized as it follows: the next section describes the experimental tensile and DCB tests that were used for the material characterization; Section 3 presents the numerical identification of the elastic parameters via genetic approach; Section 4 introduces the basics of the bi-phasic model for non-linearities and material damages; Section 5 discusses the identification through the Gaussian Process Regression method and a subsequent genetic optimization of the damage parameters and shows the numerical-experimental correlation that was achieved. The results are summarized and commented in a conclusive section.

2. Experimental tests on C/C laminates with different orientations

2.1. Tensile test campaign

The experimental data that were used for the characterization of the material under investigation were gathered in a static tensile test campaign performed on tabbed specimens. Specimens were directly cut from discs obtained from laminated preforms subject to CVI process. Since the procedure normally employed for disc lamination would have led to excessively complex and unconventional lamination sequences, special preforms were adopted to obtain the specimens for the characterization. In such preforms, the lamination sequence was modified to produce discs that allowed to obtain three groups of specimens, with partially controlled lay-ups: Chordal specimens, with fibres preferentially oriented in the direction of the applied load, Radial specimens, with fibres preferentially oriented transversally to loading direction, and Pseudo 45 specimens, which were cut from the disc to obtain fibres oriented at angles close to + 45 or − 45 degrees with respect to the applied load. The basic idea behind the adoption of these specimens was to obtain fibre-dominated responses (Chordal), shear cracking in the matrix (Pseudo 45), and transverse cracking in the matrix (Radial). Table 1 lists the lamination sequence in the central section of each specimen, thus giving an insight on the adopted lay-ups.

To reduce the influence of stress states due to load introduction, specimens were equipped with E-glass fibre-reinforced tabs, which were glued with a film of structural adhesive (3 M/AF-163–2 K) cured at 120 °C at a pressure of 4 bar. Table 1 shows the geometrical features of the three sets of specimens. Tests were carried out with an *MTS 810 – Static Test System* under displacement control, with a cross-head velocity of 1 mm/min. The load – displacement curves considered for the characterization were directly measured by the load cell and the LVDT of the

Table 1
Lamination sequences and geometrical features of C/C specimens.

Specimen Class	Lamination Sequence	Gauge length [mm]	Width [mm]	Thickness [mm]	Tabs length [mm]	Tabs thickness [mm]
Chordal	[− 32/− 52/− 4/− 24/− 44/4/− 16] [− 4/− 24/44/− 64/16/− 36/− 56] [− 12/− 32/− 52/− 4/− 24/− 44/− 64]	60	20	8	30	2.54
Pseudo 45	[− 25/− 45/− 65/− 85] [− 49/− 69/− 21/− 41] [− 45/− 65/− 85/− 37]	40	20	5	20	2.00
Radial	[86/66/− 66/94] [− 70/90/50/− 62] [66/− 66/94/74]	35	20	5	10	2.00

testing machine. In general, the overall test campaign could not be designed according to a standard because of the different shapes of the specimens that were cut from the discs and the inherent asymmetry and variability of the lay-ups, which made impossible the definition of a representative gauge length. The experience gained in previous characterizations suggested the use of the tabs to mitigate the risk of undesired failure. Strain gauges were applied to record the local strain but, due to the inhomogeneity of the material, they recorded very localized non-linear effects, which were deemed not suited for the objective of this work. For all these reasons, it was chosen to focus the correlation of the model that will be presented in Sections 3 and 4 on the response of the whole specimen using the data from load – displacement curves instead of more local information.

2.2. Results of the tensile tests

Three specimens for each class were tested. Due to the confidentiality of the material properties, the quantitative experimental results were normalized using the average load peak of chordal specimens and the corresponding average displacement. The load-displacement curves of the nine specimens involved in the experimental campaign are reported in Fig. 1. Results highlight that the maximum load and the stiffness are strongly influenced by the preferential direction of fibres, as well as the qualitative overall response of specimens.

Chordal specimens exhibited brittle or quasi-brittle responses with a noticeable dispersion of stiffness and a very large variability in the maximum load. Most of failures were localized in the vicinity of the tabs, and the typical final rupture was a diagonal fracture in the plane of specimens (see Fig. 2-A). On the contrary, Pseudo 45 specimens presented a much lower scatter in the stiffness and a moderate dispersion of strength values. After an initial linear response, the load – displacement curve was characterized by a plateau at an approximately constant load, which was followed by a drop of load carrying capability in correspondence with the development of an oblique fracture, shown in Fig. 2-B. Finally, Radial specimens showed a very limited dispersion of stiffness and maximum loads. They were characterized by a pseudo-ductile response, which was dominated by a progressive decrease of load carrying capability. The final failure was generated by the development of a fracture, which, at least in two cases, occurred in the central part of the specimen. The fracture line was always approximately perpendicular to the loading direction, as it can be seen in Fig. 2-C.

The variability of the qualitative and quantitative behaviour that was registered during the tests may be attributed to two main factors: the unconventional and unique lamination sequence of each specimen and the effect of pre-existing defects (see Fig. 3-A). The typical defects of these C/C laminates are the misalignment of laminae, the indentations left by the needling procedure, and the porosity that depends on the CVI densification.

The microscopic analysis of specimens allowed to investigate the damage mechanisms. Radial specimens were characterized by several intralaminar cracks and the failure of some groups of fibres. Delaminations were present on both Pseudo 45 (see Fig. 3-B) and Radial (see Fig. 3-C) specimens. The analysis of Pseudo 45 specimens pointed out that the heterogeneity of the orientation of fibres involved the development of widespread interlaminar cracks.

2.3. Interlaminar characterization

According to the experimental evidence, it would be impossible to develop reliable non-linear models for the structural integrity of the

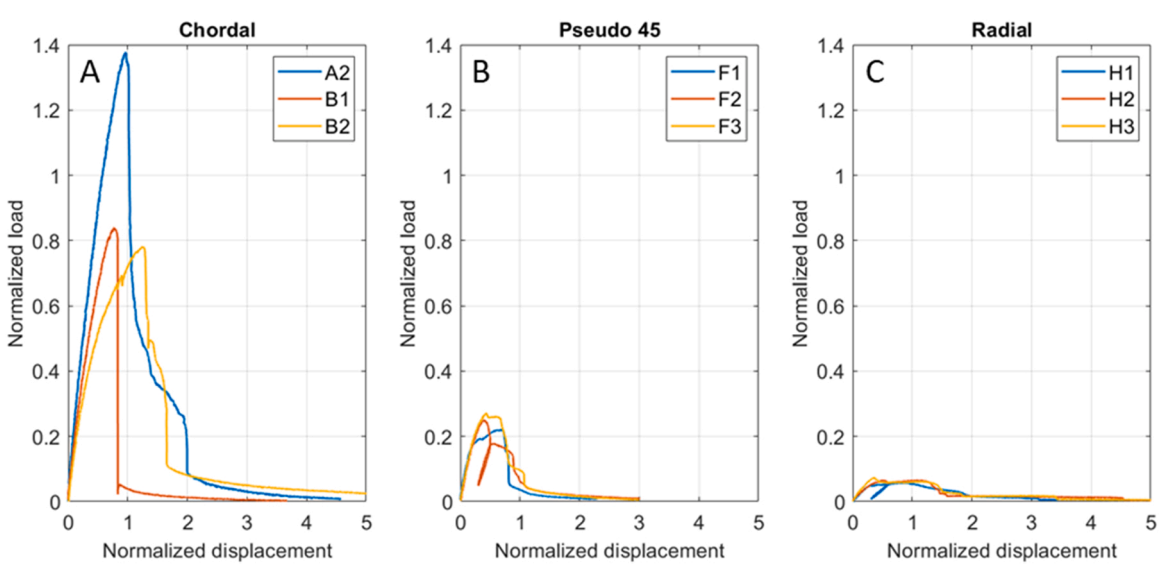

Fig. 1. Experimental tensile response of specimens: (A) Chordal, (B) Pseudo-45, (C) Radial.

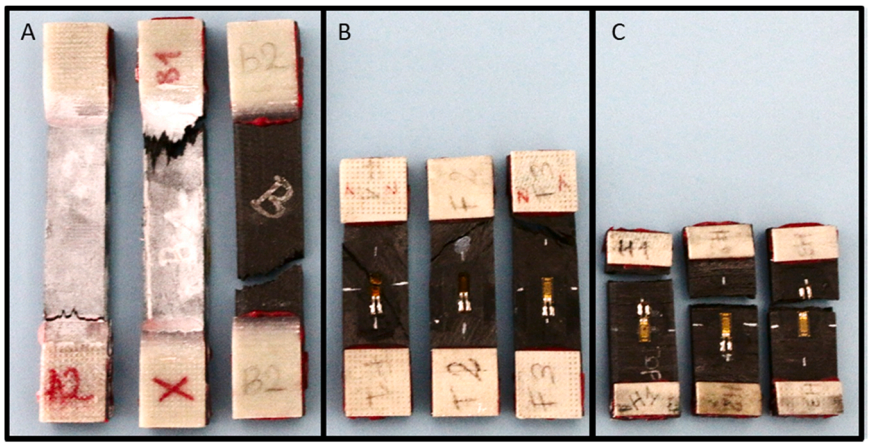

Fig. 2. Final rupture of (A) Chordal, (B) Pseudo 45 and (C) Radial.

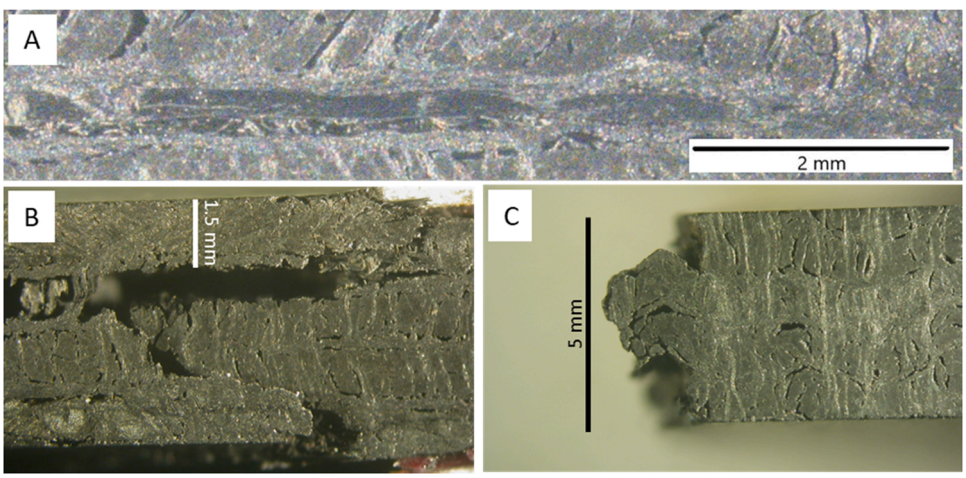

Fig. 3. Typical defects of the 2.5D C/C laminates under investigation (A) and fractures after tensile tests in a Pseudo 45 (B) and Radial (C) specimen.

thick C/C laminates under consideration without representing delamination. In general, the interlaminar properties of 2.5D C/C laminates are strongly influenced by the needling procedure, and at least a preliminary estimation of such properties was of paramount importance to develop the model. Therefore, Double Cantilever Beam (DCB) tests were performed to preliminarily assess the mode I interlaminar toughness of the material and to provide experimental data for a partial calibration of the numerical model. Tests were performed by using the ASTM standard D5528 – 13 [44] for polymeric matrix composite as a guideline, although its application to different kind of composites may require different geometrical dimensions and procedure [45–47]. The complexity of the available laminates and the uncertainty in both the lamination sequence and the interlaminar properties demanded some precautions in the design of the tests.

DCB specimens were cut from the discs used to obtain tensile specimens but, in this case, only Chordal type specimens were utilized. The geometry of the specimens, indicated as $L \times W \times H$, was $160 \times 20 \times 10.3$ mm. The significant thickness of the specimens was chosen to reduce the risk of inelastic mechanisms in the bending arms. Moreover, the lower and the upper surfaces of the specimens were reinforced by layers made of unidirectional carbon-fibres-reinforced polymer, so to further reduce the general in-plane stress state due to the bending of the arms and to mitigate the risk of inelastic mechanisms in the most compressed layers. Following the first processing of the tensile test results and preliminary DCB tests, beam theory analyses indicated that 5 mm thick tabs could guarantee that the axial stress in the C/C laminate did not exceed the 25 % of the estimated axial strength.

Since DCB specimens necessitate a pre-crack, it was required to find a technological process to cut the laminate. After some trials, it was established that water-jet-cutting followed by a pre-opening test and by an unloading of specimens could result in an adequate pre-crack length. The water-jet produced a cut with a thickness of 0.3 mm at the centre of the specimen thickness, which then evolved in a crack in the pre-opening phase of the test. As exemplified in Fig. 4-A, pre-cracks with a length in the range $a_0 = 50$ mm $\div$ 60 mm were obtained. Such length was actually obtained thanks to the installation of the load application hinges in a reverse configuration with respect to the standards, as it can be seen in Fig. 4-A. This solution was adopted due to the limited length of the specimens, which was the longest that could be obtained from discs. The tests were performed with the *MTS 810 - Static Test System* with a prescribed displacement velocity of 0.5 mm/min. A white coating (a penetrant commonly used for dye penetrant inspection) was applied to the lateral surface of specimens with the purpose of highlighting the growth of the fracture, which was photographed every 5 s by a high-definition camera. The load – displacement curves were directly obtained by the load cell and the LVDT of the testing machine, and are reported in Fig. 4-B.

Four specimens were tested, with an initial pre-crack a_0 that depended on the pre-opening phase. The slope of the linear response of specimens varied with the pre-crack length with an expected trend. Specimens DCB#1 and DCB#2, which had the same a_0 length, presented a very similar stiffness even if their lamination sequence was

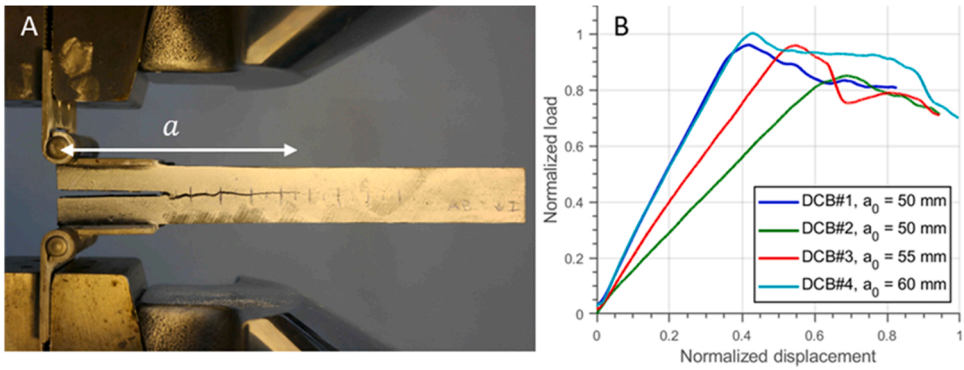

Fig. 4. DCB tests on C/C Chordal specimens: test lay-out (A) and force vs. opening response (B).

different, being they obtained from different parts of the disc. The opening of the crack triggered the gradual load decrease shown in Fig. 4-B. Cracks developed along a slightly irregular path and the surface that was exposed after the fracture showed a pronounced roughness that was a consequence of the needling process. This suggests that the friction/contact sliding between the crack faces during the crack opening, in particular in mode II, could strongly influence the forces required for the propagation of the crack. However, the investigation of such mechanism was beyond the scope of these preliminary characterization tests, which were mainly performed to evaluate the order of magnitude of the interlaminar toughness and were a first workbench for the application of the non-linear meso-scale material model.

3. Linear FE models and numerical identification of elastic parameters

3.1. Linear FE analyses

Due to the complexity of the lamination sequence of specimens, it was required an identification procedure able to perform a robust characterization of the elastic parameters of the C/C laminae. The proposed approach was based on linear FE analyses performed by using Simulia/Abaqus code, with models representing the individual unconventional lamination sequence of each specimen. The set of elastic parameters that minimized the discrepancies between numerical and experimental stiffness was identified through a genetic algorithm. The specimens were meshed with linear tetrahedral elements (C3D4) with a characteristic length of 1 mm, as exemplified in Fig. 5. The geometry was partitioned to obtain meso-scale models where each C/C UD lamina was represented by using a separate layer of tetrahedral elements. It should be observed that the layer of short fibres used for needling was not directly represented and its properties were homogenized within the ones of the C/C lamina. The response of the whole specimen, including tabs, was considered for the identification. Tabs were represented by a rough mesh of hexahedral elements, as shown in Fig. 5, characterized to represent the specific 0/90 lay-up of E-glass reinforced fabric that was used for their production. The meshes of the tabs were connected to the model of the specimen through a TIE connection algorithm, available in the solver code [48]. The external surfaces of right and left tabs were included in two different rigid bodies, and the tensile simulation was performed by keeping one of them fixed while imposing a given displacement to the other.

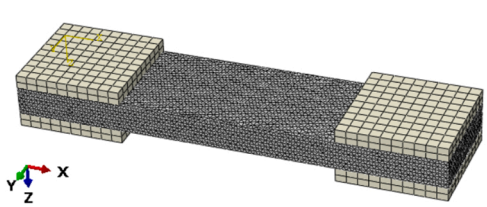

Fig. 5. FE model of a Pseudo-45 specimen.

The study was mainly aimed at identifying the parameters that define the in-plane response of the material, which are denoted as E_{11}, E_{22}, G_{12} and ν_{12}, where direction 1 is the direction of continuous fibers and direction 2 is the transversal direction in the plane of the laminae. However, a complete material characterization also necessitates the identification of the out-of-plane properties, which was carried out by introducing the assumption of transverse isotropy, that is by applying the relations $G_{13} = G_{12}$, $E_{33} = E_{22}$, and $\nu_{13} = \nu_{12}$. Although not completely adequate for the considered material, the effects of such assumption on the in-plane characterization of the material are likely to be minimal. Finally, the value of ν_{23} was fixed to 0.3, mainly to avoid non-physically admissible stiffness matrices. Hence, the set of independent variables in the identification procedure comprised E_{11}, E_{22}, G_{12}, G_{23}, and ν_{12}.

3.2. Set-up of the optimization algorithm

A genetic algorithm was applied to find the set of parameters that minimized the difference between the set of experimental and numerical stiffness of specimens. The numerical stiffness of each specimen was evaluated in a linear simulation of the tensile test considering the displacement of the rigid body connected to the moving tabs and the applied force. Then, the objective function shown in Eq. (1) assigned a scalar score to each set of material parameters, which was used to evaluate its fitness in representing the engineering constant of the plies in the C/C laminate.

$$f = \sqrt{\sum_{i=1}^{N_{spec}=9} \left(\frac{K^i_{num} - K^i_{\exp}}{K^i_{\exp}} \right)^2} \tag{1}$$

In Eq. (1), $N_{spec} = 9$ is the number of specimens, K^i_{num} is the stiffness of the i-th model evaluated in the linear analyses, and $K^i_{\exp}$ is the slope obtained through linear regressions of the first part of the force vs. displacement curve referred to the i-th specimens, i.e. one of the nine curves reported in Fig. 1.

The set of parameters was codified in a genetic code, which was generated by a genetic algorithm within the procedure summarized in Fig. 6. The material parameters were bounded inside the specific ranges indicated in Table 2, where they have been normalized with respect to the identified E_{22}, except for ν_{12} and ν_{23}. Moreover, the set of constraints formalized in Eq. (2) was introduced to discard solutions not fulfilling some reasonable assumptions regarding mutual relations between the values of the elastic parameters in the C/C material. Such constraints were directly enforced during the procedure of chromosome generation, so that they were met by every chromosome that was generated during the optimization.

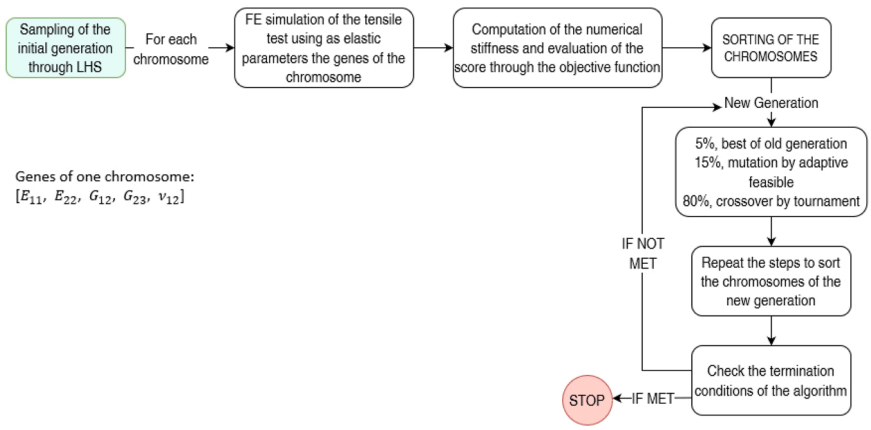

Fig. 6. Flowchart of the optimization procedure.

Table 2
Elastic parameters for the composite normalized w.r.t. E_{22}.

Parameter	Range for optimization	Identified Value
E_{11}	0 – 32.00	20.18
$E_{22} = E_{33}$	0 – ∞	1.00
$G_{12} = G_{13}$	0 – ∞	0.68
G_{23}	0 – ∞	0.23
$\nu_{12} = \nu_{13}$	0.05 – 0.35	0.27
ν_{23}	Fixed	0.30

$$\begin{cases} -E_{11} + E_{22} \leq 0 \\ -E_{22} + G_{12} \leq 0 \\ -G_{12} + G_{23} \leq 0 \end{cases} \tag{2}$$

The procedure considered a population of 100 individuals, with an initial population that was selected by sampling the admissible range of the genes by means of a Latin Hypercube Sampling (LHS). A new generation was created with the rules provided in Fig. 6. The termination conditions of the genetic algorithm were the maximum allowed number of generations (70), a tolerance on the improvement of the solution (1E-6 in terms of the objective function of Eq. (1)) and a maximum number of iterations without any modification of the best chromosome (20). The procedure was implemented through the MATLAB® built-in function *ga* [49].

3.3. Results of the optimization

The procedure ended in 34 iterations, after 20 iterations without any modification of the best chromosome, as shown in Fig. 7.

The elastic parameters of the optimal solution are reported in Table 2, with Young's and shear moduli normalized with respect to $E_{22} = E_{33}$, while Poisson's ratios are listed without any modification.

The correlation between the numerical and the experimental tensile stiffness is displayed in Fig. 8. For the sake of clarity, only one experimental curve for each class of specimens is shown, but the experimental scattering can be evaluated from the curves reported in Fig. 1. The obtained results indicate that a reliable characterization of the elastic parameters of the C/C lamina was achieved. It can be remarked that the matrix-dominated elastic moduli ($E_{22} = E_{33}$, G_{12}, G_{13}, and G_{23}) resulted at least 20 times lower than the Young's modulus in the reinforcement direction (E_{11}).

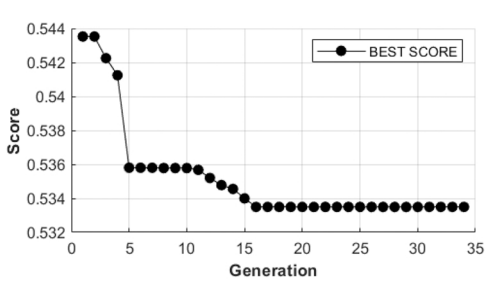

Fig. 7. Improvement of the score of the best solution.

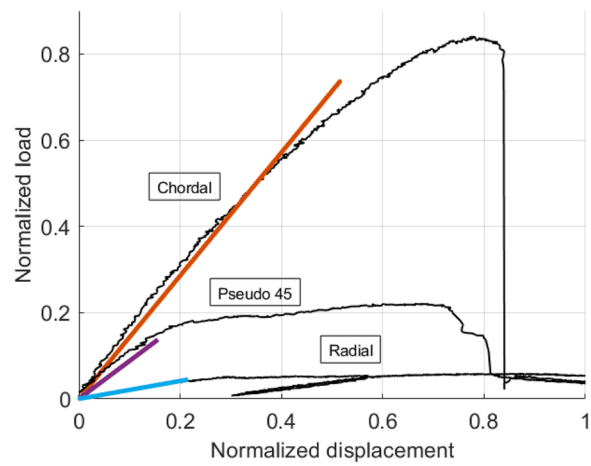

Fig. 8. Numerical correlation of the stiffness of specimens.

4. Bi-phasic model for non-linearity and failure

4.1. General concepts for the development of the bi-phasic model with hybrid mesh

The development of a model for the non-linear response and failure was pursued by modelling C/C laminates with the approach proposed in [23], which is a kind of binary model based on a bi-phasic decomposition of the properties of the composite. The decomposition produces an idealized fibre phase, representing the continuity of the reinforcement, and an effective medium for matrix, representing the matrix-dominated responses of the laminate. Moreover, a hybrid modelling technique with different types of elements for the two phases is adopted. The main advantages of this technique, which were claimed and demonstrated in [23], are related to the development of models capable of representing delaminations, matrix damages, fibre damages and their interactions reducing the computational time and avoiding the introduction of non-physical parameters in the material properties with respect to more conventional approaches.

In the bi-phasic decomposition, which is not a micromechanical model, the idealized fibre phase carries only stress in the reinforcement direction, so that it is not defined to represent the physical fibre phase into the composite. The two phases share the same volume and are subjected to the same strain, as it is apparent from the constitutive model in the elastic range represented in Eq. (3).

$$\sigma^{Comp} = \sigma^f + \sigma^m = \left(D^f + D^m\right)\varepsilon \tag{3}$$

Considering that E^{f-eff} is the effective Young's modulus of fibres and that V^f their volumetric fraction, Eq. (3) can be conveniently written as Eq. (4) to highlight the different stiffness contribution of each idealized phase.

$$\begin{bmatrix} \sigma_{11} \\ \sigma_{22} \\ \sigma_{33} \\ \tau_{12} \\ \tau_{23} \\ \tau_{31} \end{bmatrix} = \left(\begin{bmatrix} E^{f-eff}V_f & 0 & 0 & 0 & 0 & 0 \\ 0 & 0 & 0 & 0 & 0 & 0 \\ 0 & 0 & 0 & 0 & 0 & 0 \\ 0 & 0 & 0 & 0 & 0 & 0 \\ 0 & 0 & 0 & 0 & 0 & 0 \\ 0 & 0 & 0 & 0 & 0 & 0 \end{bmatrix} + \begin{bmatrix} D^m_{11} & D^m_{12} & D^m_{13} & 0 & 0 & 0 \\ D^m_{21} & D^m_{22} & D^m_{23} & 0 & 0 & 0 \\ D^m_{31} & D^m_{32} & D^m_{33} & 0 & 0 & 0 \\ 0 & 0 & 0 & D^m_{44} & 0 & 0 \\ 0 & 0 & 0 & 0 & D^m_{55} & 0 \\ 0 & 0 & 0 & 0 & 0 & D^m_{66} \end{bmatrix} \right) \begin{bmatrix} \varepsilon_{11} \\ \varepsilon_{22} \\ \varepsilon_{33} \\ \gamma_{12} \\ \gamma_{23} \\ \gamma_{31} \end{bmatrix} \tag{4}$$

The two phases are then characterized by different non-linear responses based on Cohesive Zone Models (CZM), thus distinguishing fibre-dominated and matrix dominated responses, as it will be shown in the subsequent subsection. Moreover, thanks to the adopted hybrid modelling technique, in the matrix phase CZM will be used to represent both intralaminar damage and delamination without the need of interface elements.

One of the issues that needs to be addressed is the development of a proficient decomposition procedure, i.e. a procedure that moves from the elastic parameters of the composite materials, which were identified in Section 3, and define the parameters of the idealized phases. Despite the plainness of the decomposition represented in Eq. (4), it is important avoiding non-physically admissible properties for the matrix phase and obtaining, at the same time, a reasonable approximation of the contribution of the fibres in the reinforcement direction [50]. The procedure developed in [23,50] for bi-phasic models provides the possibility of a direct identification of suitable properties for the fibre and matrix phases. The application of such procedure to the stiffness properties of the C/C laminae resulted in the normalized values that are listed in Table 3. It is noted that the decomposition led to a very stiff fibres-phase surrounded by a compliant matrix-phase, with a ratio E^f_{11}/E^m_{11} of around 26.

A second fundamental aspect of the modelling technique is the adoption of a hybrid mesh comprising two different types of elements for the fibre and the matrix phases. The stiffness attributed to the idealized fibres-phase is concentrated at the mid-planes of the plies constituting the laminate and it is represented within membrane elements, whereas the effective medium idealized by the matrix-phase is used to characterize solid elements that connect the membranes. Hence, the hybrid mesh consists of 4-noded membrane elements located on the mid-planes of the laminae and connected by 8-noded under-integrated hexahedral elements. Damage laws in the element representing the idealized matrix phase can be used to represent delamination, matrix cracking and their interactions. Membrane and hexahedral elements share the same nodes and both adopt linear interpolation functions, thus guaranteeing compatibility. In the technique described in [23], membrane elements are located on the midplane of each lamina. However, given that the C/C laminae under consideration are significantly thick (more than 1 mm), each physical lamina was divided in three sub-laminae – or sub-plies – on whose mid-planes membrane elements were located. This led to an adequate through-the-thickness mesh refinement and produced a mesh in which some connection elements belonged to the same physical lamina, whereas others were set between two adjacent laminae and were defined as interlaminar layers (see Fig. 9).

Table 3
Elastic parameters after decomposition normalized w.r.t. E_{22} of the composite.

Parameter	Value
E^f_{11}	23.12
$E^m_{11} = E^m_{22} = E^m_{33}$	0.88
G^m_{12}	0.77
$G^m_{13} = G^m_{23}$	0.61
$\nu^m_{12} = \nu^m_{13}$	0.30
ν^m_{23}	0.19

4.2. Constitutive laws in the elastic range for the matrix elements between differently oriented plies

Before introducing the approach to model fibre and matrix damage modes, the constitutive law in the elastic range for the matrix deserves additional attention. The modelling technique presents a specific issue related to the fact that the solid elements contain the matrix phase of the two adjacent sub-plies that they connect, which will be referred to as semi-phases. In the case of connection elements that are placed at interlaminar layers, the semi-phases have, in general, two different reinforcement orientations: the one of the upper (U) and the one of the lower (L) physical lamina. This aspect is addressed in the constitutive law of the matrix-phase, which computes the response of connection elements as the combination of the two semi-phases that they embody. In the following discussion, the constitutive law is expressed in the element reference frame (x, y, z) whereas the properties of the semi-phases are in the material reference frame $(1, 2, 3)$, where 1 is along the reinforcement direction and z and 3 are along the thickness of the laminate (see Fig. 10). In the adopted formulation, the matrix semi-phases were characterized by the reinforcement orientations θ^U and θ^L and by the thickness ratios α^U and α^L. Thickness ratios were defined as $\alpha^{U,L} = t^{U,L}/2t$, where $t^{U,L}$ is the thickness of the upper or lower sub-ply and t is the thickness of the solid element. The stress and the strain acting in the two semi-phases included in the matrix element will be denoted as $\sigma^{U,L}_{ij}$ and $\varepsilon^{U,L}_{ij}$, respectively.

According to equilibrium considerations, the out-of-plane stress components that are transmitted through the interface can be reasonably assumed to be equal in the two matrix semi-phases, so that $\sigma^U_{33} = \sigma^L_{33} = \sigma^m_{zz}$. The out-of-plane strains of the two semi-phases depend on the stress state in the semi-phases and on the specific material properties. The out-of-plane strain of the whole element can be evaluated as the

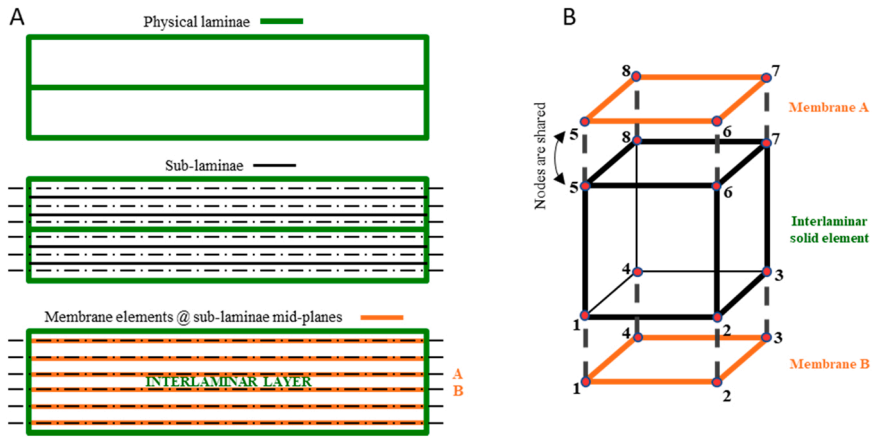

Fig. 9. Scheme of the hybrid mesh adapted to the C/C laminates (A) and detail of elements involved in an interlaminar layer between two different laminae (B).

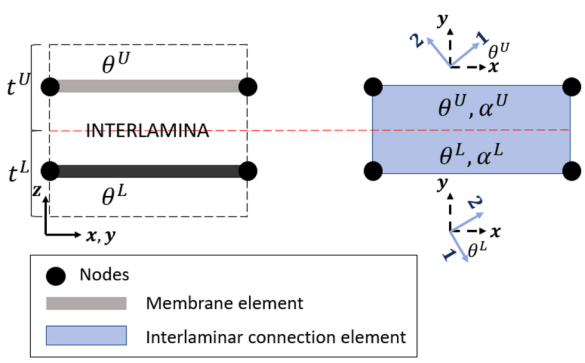

Fig. 10. Material and element reference frames.

$$E_{zz}^{eq} = \frac{E_{33}^{U} E_{33}^{L}}{\alpha^{U} E_{33}^{L} + \alpha^{L} E_{33}^{U}} \tag{7}$$

Similar considerations lead to the formulation of the out-of-plane equivalent shear moduli (see Eq. 8).

$$G_{yz}^{eq} = \frac{2G_{23}^{U} G_{33}^{L}}{\alpha^{L} G_{23}^{U} + \alpha^{U} G_{23}^{L}}; G_{xz}^{eq} = \frac{2G_{13}^{U} G_{13}^{L}}{\alpha^{L} G_{13}^{U} + \alpha^{U} G_{13}^{L}} \tag{8}$$

Regarding the in-plane stress components, it is assumed that the semi-phases are subject to the same in-plane strain state, which means that $\varepsilon_{xx}^{m} = \varepsilon_{xx}^{U} = \varepsilon_{xx}^{L}$, $\varepsilon_{yy}^{m} = \varepsilon_{yy}^{U} = \varepsilon_{yy}^{L}$ and $\gamma_{xy}^{m} = \gamma_{xy}^{U} = \gamma_{xy}^{L}$. These strain components are conveniently rotated in the material reference frame to compute the in-plane stress of the semi-phases. The form reported Eq. (9) is referred to the response in the elastic range for each semi-phase.

$$\begin{cases} \sigma_{11}^{U,L} = E_{11}^{U,L}\left[\left(1-\nu_{23}^{U,L}\nu_{32}^{U,L}\right)Y^{U,L}\varepsilon_{11}^{U,L} + \left(\nu_{21}^{U,L}+\nu_{31}^{U,L}\nu_{23}^{U,L}\right)Y^{U,L}\varepsilon_{22}^{U,L} + \left(\nu_{31}^{U,L}+\nu_{21}^{U,L}\nu_{32}^{U,L}\right)Y^{U,L}\varepsilon_{33}^{U,L}\right] \\ \sigma_{22}^{U,L} = E_{22}^{U,L}\left[\left(\nu_{12}^{U,L}+\nu_{13}^{U,L}\nu_{32}^{U,L}\right)Y^{U,L}\varepsilon_{11}^{U,L} + \left(1-\nu_{31}^{U,L}\nu_{13}^{U,L}\right)Y^{U,L}\varepsilon_{22}^{U,L} + \left(\nu_{32}^{U,L}+\nu_{31}^{U,L}\nu_{12}^{U,L}\right)Y^{U,L}\varepsilon_{33}^{U,L}\right] \\ \tau_{12}^{U,L} = G_{12}^{U,L}\gamma_{12}^{U,L} \end{cases}$$

weighted sum of the strains of the two semi-phases. Such considerations lead to the relations in Eq. (5).

$$\begin{aligned} \varepsilon_{33}^{U,L} &= \frac{1}{E_{33}^{U,L}}\sigma_{zz}^{m} - \frac{\nu_{13}^{U,L}}{E_{11}^{U,L}}\sigma_{11}^{U,L} - \frac{\nu_{23}^{U,L}}{E_{11}^{U,L}}\sigma_{22}^{U,L} \\ \varepsilon_{zz}^{m} &= \alpha^{U}\varepsilon_{33}^{U} + \alpha^{L}\varepsilon_{33}^{L} \end{aligned} \tag{5}$$

The out-of-plane stress σ_{zz}^{m} can be expressed in terms of the out-of-plain strain ε_{zz}^{m} and of the in-plane stress components by combining and inverting the relations in Eq. (5). The resulting expression of Eq. (6) for σ_{zz}^{m} gives the opportunity to introduce an equivalent out-of-plane modulus, defined in Eq. (7).

$$\sigma_{zz}^{m} = \left(\frac{E_{33}^{U}E_{33}^{L}}{\alpha^{U}E_{33}^{L} + \alpha^{L}E_{33}^{U}}\right)\left[\varepsilon_{zz}^{m} + \alpha^{U}\left(\frac{\nu_{13}^{U}}{E_{11}^{U}}\sigma_{11}^{U} + \frac{\nu_{23}^{U}}{E_{22}^{U}}\sigma_{22}^{U}\right) + \alpha^{L}\left(\frac{\nu_{13}^{L}}{E_{11}^{L}}\sigma_{11}^{L} + \frac{\nu_{23}^{L}}{E_{22}^{L}}\sigma_{22}^{L}\right)\right] \tag{6}$$

$$Y^{U,L} = \frac{1}{1-\nu_{12}^{U,L}\nu_{21}^{U,L} - \nu_{23}^{U,L}\nu_{32}^{U,L} - \nu_{13}^{U,L}\nu_{31}^{U,L} - 2\nu_{21}^{U,L}\nu_{32}^{U,L}\nu_{13}^{U,L}} \tag{9}$$

It can be observed that the evaluation of $\sigma_{11}^{U,L}$ and $\sigma_{22}^{U,L}$ completes the information required in Eq. (6) to compute the out-of-plane stress state. Then, the two sets of stress components are rotated backward in the reference frame of the matrix element and combined in the element reference frame by a modified rule of mixtures to compute the overall in-plane stress (see Eq. 10).

$$\begin{cases} \sigma_{xx}^{m} = \dfrac{\alpha^{U}\sigma_{xx}^{U} + \alpha^{L}\sigma_{xx}^{L}}{F_{33}} \\ \sigma_{yy}^{m} = \dfrac{\alpha^{U}\sigma_{yy}^{U} + \alpha^{L}\sigma_{yy}^{L}}{F_{33}} \\ \tau_{xy}^{m} = \dfrac{\alpha^{U}\tau_{xy}^{U} + \alpha^{L}\tau_{xy}^{L}}{F_{33}} \end{cases} \tag{10}$$

where F_{33} is the third term on the diagonal of the deformation gradient evaluated at the integration point of the element. The term F_{33} constitutes a required correction for the thickness ratios α^U and α^L, which avoids errors in the evaluation of the in-plane stress when a solid connection element experiences large out-of-plane deformation, as in the case of delamination [23].

Both the out-of-plane and the in-plane constitutive laws are suitable for the embedment of damage laws based on scalar damage variables. In the case of the out-of-plane law, the damage variable degrades the equivalent moduli E_{zz}^{eq}, G_{yz}^{eq} and G_{xz}^{eq}, expressed in Eq. (7) and Eq. (8), representing the loss of stress transmission capability of the interface of two adjacent plies due to delamination. On the other hand, the deterioration through another damage variable of $E_{22}^{U,L}$, $G_{12}^{U,L}$ and of Poisson's ratios $\nu_{12}^{U,L}$ and $\nu_{23}^{U,L}$ models the effects of matrix damage within the laminae. Two damage variables for out-of-plane and matrix cracking damage, namely d_{mo} and d_{mc}, were defined with evolution laws based on Cohesive Zone Models (CZM) embedded in the solid elements, as it is discussed in the next subsection.

4.3. Cohesive zone models for matrix cracking and delamination

In the model proposed for C/C material, CZMs were adopted to represent both delamination and matrix cracking in the elements that embody the matrix phase. CZMs are typically expressed in the form of traction-separation laws to represent both the strength and the toughness of an interface undergoing fracture process. In finite element models, such laws are usually implemented in zero or infinitesimal thickness cohesive elements, representing the interface, which must be characterized by very high penalty stiffness to avoid unrealistic response before fracture onset [29]. In this work, two CZMs are embedded in 8-noded hexahedral solid elements having a reduced integration scheme and single integration point, especially suited for FE analyses with an explicit time integration scheme. These elements are the connection elements representing the matrix phase, and the embedment of CZMs into finite thickness elements avoids the need of using zero-thickness interface elements throughout the volume of the composite, which would involve node duplication and the numerical issues related to the presence of very high penalty stiffness (see [34,36,38]). However, the embedment of CZMs into solid elements requires the introduction of a regularization distance related to the dimension of elements, which should be considered an additional material parameter. A comparison between an approach based on interface element and the approach proposed is exemplified in Fig. 11, referred to a fracture occurring along an interface in the x-y plane between the parts A and B of a solid continuum.

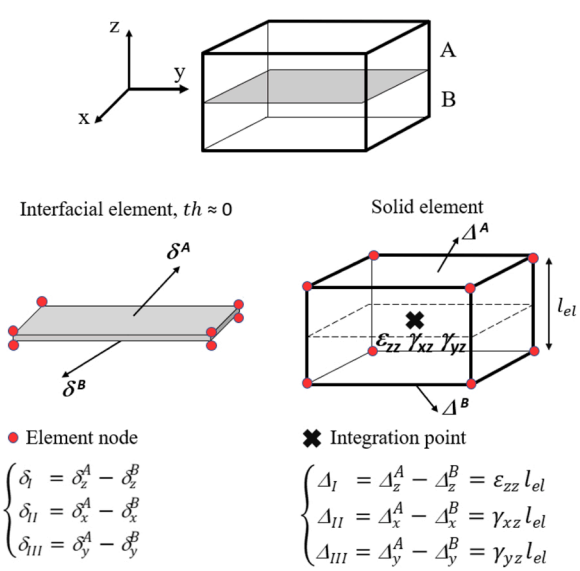

Fig. 11. Implementation of CZM in interface and solid elements.

The conventional cohesive element describes the fracture in terms of discontinuities at such interface through the vectors δ^A and δ^B, which are used to define the separation variables in different modes, δ_I, δ_{II} and δ_{III}. In a CZM embedded into a solid element, the fracture process in the x-y plane is smeared in the volume of the element. The energy spent in crack development can be related to finite displacements (Δ^A and Δ^B) between the element faces. The relative displacements can be classified according to the opening mode that they involve (Δ_I, Δ_{II}, or Δ_{III} defined in Fig. 11). Within the assumption of small displacements, the relative displacements are linked in Fig. 11 to the average strain components ε_{zz}, γ_{xz} and γ_{yz} in the solid by introducing the element length l_{el}. The element length plays the role of regularization distance in the definition of a damage model embedded in a solid [51]. The toughness related to the fracture process can now be expressed in terms of the stress-strain relation as in Eq. (11):

$$\begin{cases} G_{Ic} = \int_0^\infty \sigma_I d\Delta_I = l_{el} \int_0^\infty \sigma_I(\varepsilon_{zz}) d\varepsilon_{zz} \\ G_{IIc} = \int_0^\infty \sigma_{II} d\Delta_{II} = l_{el} \int_0^\infty \sigma_{II}(\gamma_{xz}) d\gamma_{xz} \\ G_{IIIc} = \int_0^\infty \sigma_{III} d\Delta_{III} = l_{el} \int_0^\infty \sigma_{III}(\gamma_{yz}) d\gamma_{yz} \end{cases} \tag{11}$$

where σ_I, σ_{II} and σ_{III} are the equivalent stresses obtained from the stress tensor in the element, which will be defined later. It is worth noting that the adoption of under-integrated hexahedral elements as connection elements in the hybrid approach described in Section 4.1 provides, at the single integration point of the element, the average stress and strain state in the volume required by Eq. (11). The relations expressed in Eq. (11) must be fulfilled by the stress-strain law that characterizes the response of the material during the opening of a fracture in a pure mode. Such response is shaped by the evolution of a damage variable.

Although the typical choice for a pure mode response in a CZM is based on bi-linear laws [29], a more complex response was adopted to represent the progressive damage accumulation and the "graceful failure" of C/C material. In particular, it was defined a tri-linear response obtained by superimposing two bi-linear (triangular) responses, denoted by indices b and d in Fig. 12. This approach was suggested in [52,53] to model delamination processes characterized by significant process zones and a consequent R-curve effect. Considering a generic opening mode, the maximum stress that can be carried by the interface, σ_0, and the total toughness, G_c, are distributed between the two superimposed bi-linear responses by means of two shape parameters m and n, with $0 \le m$, $n \le 1$, such that $\sigma_0^b/\sigma_0 = n$ and $G_c^d/G_c = m$. The bi-linear responses and

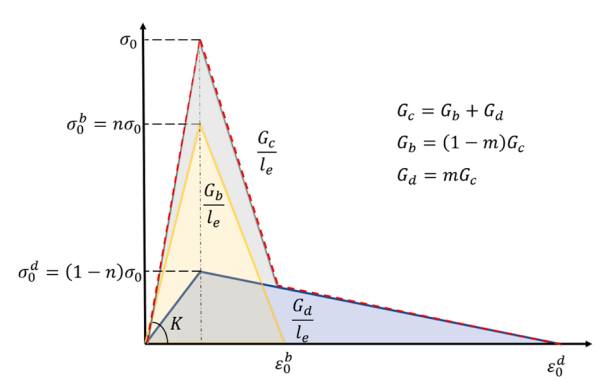

Fig. 12. Trilinear response of the cohesive law.

Table 4
Cohesive laws parameters for out-of-plane and in-plane damage.

	CZM for delamination	CZM for transverse cracking
Equivalent strain	$\varepsilon_I = \begin{cases} 0 if \varepsilon_{33} \le 0 \\ \varepsilon_{33} if \varepsilon_{33} > 0 \end{cases} \quad \varepsilon_{II} = \sqrt{\gamma_{13}^2 + \gamma_{23}^2}$	$\varepsilon_I = \begin{cases} 0 if \varepsilon_{22} \le 0 \\ \varepsilon_{22} if \varepsilon_{22} > 0 \end{cases} \quad \varepsilon_{II} = \lvert\gamma_{12}\rvert$
Equivalent stress	$\sigma_I = \begin{cases} 0 if \sigma_{33} \le 0 \\ \sigma_{33} if \sigma_{33} > 0 \end{cases} \quad \sigma_{II} = \sqrt{\tau_{13}^2 + \tau_{23}^2}$	$\sigma_I = \begin{cases} 0 if \sigma_{22} \le 0 \\ \sigma_{22} if \sigma_{22} > 0 \end{cases} \quad \sigma_{II} = \lvert\tau_{12}\rvert$
Regularization length	Distance between the mid-planes of sub-laminae	Length of the element in the direction orthogonal to fibres
Degraded Parameters	$E_{zz}^{eq}, G_{xz}^{eq}, G_{yz}^{eq}$	$E_{22}^{U,L}, G_{12}^{U,L}, \nu_{12}^{U,L}, \nu_{23}^{U,L}$

the resulting tri-linear curve are represented in Fig. 12. To avoid further complication in the model, the parameters m and n are common for all the opening modes represented in the CZM.

Finally, the work presented in [54] was used as a groundwork to develop CZMs that were capable of modelling mixed-mode scenarios by including quadratic strength and toughness criteria. The algorithms for the treatment of mixed modes were applied to both the bi-linear responses that compose the tri-linear behaviour, thus obtaining a tri-linear response in mixed mode that fulfilled the adopted strength and toughness criteria.

In this work, the previous scheme was applied to develop two different CZMs that were implemented in the constitutive law of the solid connection elements embodying the idealized matrix phase. These CZMs were used to model both the intra- and the inter-laminar damage, that is delamination and matrix cracking, which were described by two scalar damage variables, d_{mo} and d_{mc}. Two scalar variables were actually required for matrix cracking: d_{mc}^U for the upper semi-phase and d_{mc}^L for the lower one. Moreover, it was assumed that delamination cannot occur within the same physical ply, so that the delamination model was activated only in the interlaminar layers of the hybrid mesh, defined in Fig. 9-B.

The two models were implemented through the same algorithm described above, but they differ for the definition of the two equivalent strains (ε_I and ε_{II}) and the two corresponding equivalent stresses (σ_I and σ_{II}) that were used to describe delamination and transverse cracking inside the matrix element. Considering a constitutive model defined in a material reference frame, where 1 is direction of fibre reinforcement, 2 is the transversal direction in the lamina plane, and 3 is the out-of-plane direction, Table 4 reports the definition of the equivalent stresses and strains measures for the two different CZMs. Moreover, the characteristic element lengths that were adopted in the formulation are reported, as well as the elastic parameters affected by damage variables. It can be observed that, for the delamination model, the assumption of equivalence between mode II and mode III was introduced (as in [54]), so that the equivalent stress and strain for mode II were defined as a combination of out-of-plane shear stresses and strains. For the transverse cracking model, mode II was driven only by the in-plane shear stress and strain, while mode III was not defined.

Accordingly, the damage model for the matrix phase required 12 parameters, namely T_{22} and S_{12}, which are the intralaminar strength in mode I and mode II, $G_{Ic-intra}$ and $G_{IIc-intra}$, which are the corresponding toughness, m_{intra} and n_{intra}, which define the tri-linear cohesive response, T_{33}, $S_{13} = S_{23}$, referred to the interlaminar strength in mode I and mode II, $G_{Ic-inter}$, $G_{IIc-inter}$, m_{inter} and n_{inter}, which define the toughness properties and the tri-linear responses for the interlaminar damage phenomena.

Moreover, the possibility to represent the effect of transverse cracking on the development of delamination in the constitutive law of the matrix element was exploited. Such effect is documented by several authors for long fibre reinforced composites [55–58], but a reliable model with conventional cohesive elements would require representing complex stress fields in the vicinity of cracks at sub-millimetric scale. However, in the present approach delamination and transverse cracking were described within the same element and the effect of transverse cracks on the potential development of delamination was introduced by coupling the out-of-plane and the in-plane matrix damage variable. This was achieved by modifying the interlaminar strength and toughness in mode II depending on the intralaminar matrix damage variables, as shown in Eq. (12):

$$\widetilde{S}_{13} = \left(1 - h\max\left(d_{mc}^U, d_{mc}^L\right)\right) S_{13}$$

$$\widetilde{G}_{II-inter} = \left(1 - h\max\left(d_{mc}^U, d_{mc}^L\right)\right) G_{II} \tag{12}$$

According to Eq. (12), the definition of a coupling parameter h, with $0 \le h \le 1$, leads to a reduction of strength and toughness for shear-mode delamination in the presence of a matrix damage in the adjacent plies.

Finally, the constitutive law for fibres was attributed to membrane elements. The inelastic effects were modelled through a bi-linear cohesive law associated to another scalar damage variable d_f. The fibre damage is activated once that the threshold stress σ_0^f is reached in the fiber phase, and the bi-linear response is completely defined by assigning the final strain ε_F^f at which d_f reaches 1, meaning a complete failure of fibres. Hence, a total number of 15 material parameters was required for the definition of the non-linear response of the C/C material.

Both the constitutive law for the matrix, including the in-plane and out-of-plane CZMs, and the one of fibres were implemented in a Fortran *vumat* subroutine for the Abaqus Explicit code. Such laws were used to characterize the response of hexahedral solid elements and membrane solid elements in the hybrid and bi-phasic model of the C/C. It is worth observing that avoiding zero-thickness interface elements brings a fundamental advantage in explicit analyses, since the high penalty stiffness of interface elements has a detrimental effect on the stable time increment required to perform the analyses, thus leading to a great increment of the computational time with respect to the proposed technique [36].

4.4. Numerical simulation of DCB tests

The binary technique presented in the previous subsection was firstly applied to simulate the DCB tests described in Section 2. The numerical analyses allowed to determine the material toughness and strength in mode I through a sensitivity analysis. Since in DCB specimens the crack follows a pre-determined path, the coupon was modelled through continuum shells (Elements SC8R in [48]) except for the two core laminae interested by delamination, which were modelled with the hybrid bi-phasic technique by using six layers of M3D4R membrane elements [48] (three for lamina) connected by C3D8R hexahedral elements [48] representing the idealized matrix phase. The element size along the longitudinal axis of the specimen was set to 1 mm. The hinges shown in Fig. 4 were modelled through rigid bodies with a motion determined by two reference nodes, which were assigned proper boundary conditions including a smoothly and progressively increasing velocity to perform a quasi-static simulation with the Simulia/Abaqus Explicit solver.

The contour of the out-of-plane damage and the correlation between the numerical load-displacement curves and one experimental curve are shown in Fig. 13. The toughness $G_{Ic-inter}$ and the parameters m_{inter} and n_{inter} were changed until the experimental response after the crack onset

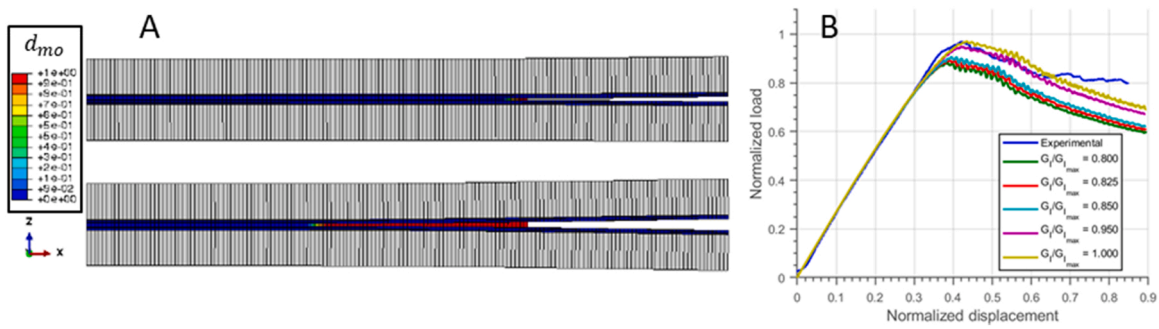

Fig. 13. Qualitative (A) and quantitative (B) correlation between numerical and experimental DCB tests.

Table 5
Normalized interlaminar parameters calibrated through the simulation of DCB tests.

Parameter	Result of calibration
$G_{Ic-inter}$	1.00
$G_{IIc-inter}$	3.85
T_{33}	0.68
m_{inter}	0.20
n_{inter}	0.75

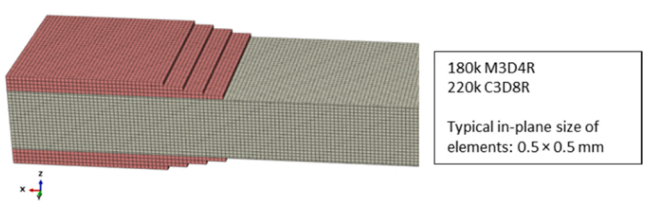

Fig. 14. Numerical model of a chordal specimen.

was matched. The simulation of the DCB test does not allow a precise identification of the interlaminar strength T_{33}, but its value was fixed to a level that did not affect the correlation, since excessively high values can alter the numerical response at the crack onset.

It can be observed that the final correlation between numerical and experimental trends is significant, although the experimental scattering is not negligible, as it can be seen from Fig. 4. Once the toughness in mode I was established, the one in mode II was approximate so that $G_{IIc-inter}$ was around 4 times greater than $G_{Ic-inter}$, considering that typically $G_{II} > G_I$ for composite materials. It was assumed that the uncertainty on the precise value of $G_{IIc-inter}$ would have not affect the results of the simulation of the tensile specimens, which was the focus of the overall activity. The parameters identified through these DCB simulations are listed in Table 5. In the table, T_{33} was normalized using the value of S_{13} identified in Section 5, while the parameters related to toughness were normalized with the value of $G_{Ic-inter}$.

The value of interlaminar damage onset $S_{13} = S_{23}$, which is also affected by the coupling law expressed in Eq. (11), was left among the parameters to be identified by means of tensile test simulations as well as the coupling term h, defined in Eq. (12), which model the reduction of interlaminar strength and toughness in the presence of intralaminar damage.

5. Numerical identification of the non-linear material model for in-plane response

This section describes the numerical identification of the parameters that define the non-linear response of the material, which are the material model parameters that have been introduced in the previous section. Exceptions are the ones modelling the interlaminar toughness and strength in mode I ($G_{Ic-inter}$, T_{33}), the interlaminar toughness in mode II ($G_{IIc-inter}$) and the shape parameters m_{inter} and n_{inter}, which were fixed after the simulation of the DCB test. The total number of parameters considered in the identification was therefore 12.

All the nine tensile specimens were modelled according to the bi-phasic approach: the idealized matrix phase was meshed using C3D8R elements, whereas M3D4R elements were used for the idealized fibre phase. The model included butt-joints, which are zones where laminae were interrupted in the preforms. Such regions were simply modelled by removing the membrane elements representing the fibres and leaving the matrix alone. Models also included the reinforcement tabs represented by C3D8R elements with a linear elastic behaviour, connected to the mesh of the specimens by using the same nodes. Fig. 14 shows the model of a Chordal specimen near the tabs and provides the basic information about the mesh.

The explicit analyses were performed by applying a progressively increasing velocity to the rigid bodies created on the surface of the moving tabs and were sped-up by adding artificial mass, according to the mass scaling technique typically adopted in quasi-static explicit FE analyses [33–37,48,56], checking that, according to energy balance and equilibrium of reaction forces, the simulation of the tensile tests occurred under quasi-static conditions.

5.1. Definition of metamodels and objective function

The complex lamination sequences and the damage scenarios that characterized the tensile test campaign led to develop an automatic method for the identification of the material parameters. However, a direct application of an optimization procedure, like in the case of the identification of the elastic parameters reported in Section 3, would have required a very large number of non-linear analyses with unacceptable computational costs. For such a reason a technique based on meta-models was implemented. In particular, a surrogate model was developed by using a database of numerical results, through the supervised learning tool of MATLAB® called *GPR Matérn 5/2* [59]. This meta-model allowed to estimate the value of different objective functions associated to a chromosome composed by a given set of damage parameters without directly performing the non-linear analyses. Hence, the required non-linear analyses were reduced to the ones needed to define the database used to produce the metamodel of the selected objective function. The approach allowed exploring different possibilities for the definition of the objective function, which was fundamental to achieve an acceptable numerical-experimental correlation.

A further reduction of the computational cost was obtained by choosing to build the database by selecting only one specimen for each class. In particular, specimens B1, F3 and H2 were chosen. After some attempts, an effective objective function was selected, which considered the combination of two indicators for each specimen: the maximum force observed during the tensile test and the area under the load-displacement curve. The curves reported in Fig. 15-A illustrate, for the selected specimens, the indicators employed to define metamodels.

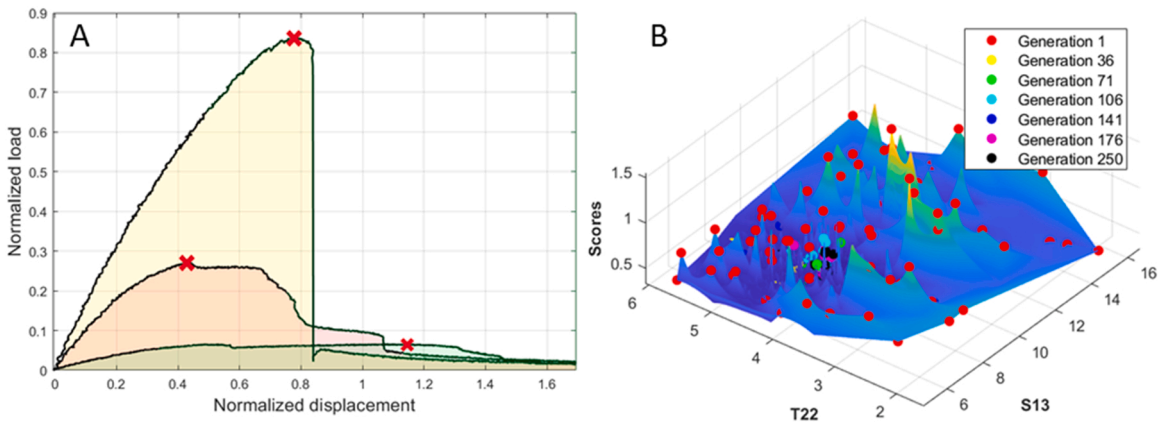

Fig. 15. Indicators that define the correlation between numerical and experimental curves (A) and section of the meta-model of the selected objective function for a variation of S_{13} and T_{22}(B).

Table 6
Range of sampling and optimal normalized damage parameters in the identification of material model.

Parameter	Initial range	Refined range after additional sampling	Identified parameters
S_{13}	0.46–1.83	0.72–1.21	1.00
h	0.00–1.00	0.00–0.01	0.63
T_{22}	0.49–0.68	0.49–0.68	0.49
S_{12}	0.46–1.83	0.46–1.83	0.95
$G_{Ic-intra}$	0.03–0.51	0.03–0.51	0.38
$G_{IIc-intra}$	1.28–3.85	1.28–3.85	1.70
m_{intra}	0.05–0.50	0.05–0.50	0.40
n_{intra}	0.50–0.95	0.50–0.95	0.86
σ_0^f	1.78–8.89	2.66–3.10	3.03
ε_F^f	1.76–17.64	1.76–17.64	10.14

Eq. (12) illustrates the objective function for the identification of damage parameters, where A^i indicates the area under the load-displacement curve and P^i the maximum load for each specimen and the corresponding numerical model.

$$f = \sqrt{\sum_{i=1}^{N_{spec}=3} \left(\left(\frac{A^i_{num} - A^i_{exp}}{A^i_{exp}} \right)^2 + \left(\frac{P^i_{num} - P^i_{exp}}{P^i_{exp}} \right)^2 \right)} \tag{12}$$

The embedment of CZM into finite-dimension elements required the introduction of the following constraints on the damage variables, which are necessary to obtain admissible CZMs:

$$T_{22}^2 < \frac{2mG_I E_{22}}{n \quad l_{el}} \tag{13}$$

$$S_{12}^2 < \frac{2mG_{II} G_{12}}{n \quad l_{el}} \tag{14}$$

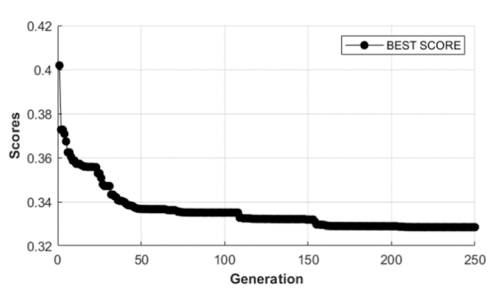

Fig. 16. Best score evolution during the identification of damage parameters.

$$\frac{\sigma_0}{C^f_{1111}} < \varepsilon_0^f \tag{15}$$

Eqs. (13) and (14) guarantee that the energy that is required to completely deteriorate one element, respectively in the intralaminar mode I and mode II, is greater than the energy accumulated in the elastic domain, which depends on the characteristic element length l_{el}. In a similar way, Eq. (15) ensures that the strain at damage initiation for the fibres is smaller than the strain at ultimate failure.

For the build-up of the database, the domain of the material parameters was sampled through a Latin Hypercube Sampling, which occurred in two steps. In a preliminary step, the database was built by using 90 combinations of material model parameters. The aim of this preliminary phase was identifying a restricted domain for some fundamental parameters, such as S_{13} and σ_0^f, where good solutions concentrated (see for example Fig. 15-B). In the restricted domain selected after the preliminary analyses, 90 additional combinations were sampled, so that the final database for the meta-models was constituted by 180 non-linear analyses. The meta-models were verified by comparing their output with the one obtained through Abaqus/Explicit for 20 combinations of genes not involved in their development.

The optimization procedure for the damage properties was carried out using the meta-models and imposing the same parameters and termination conditions employed for the elastic constants (see Section 3), but the number of maximum iterations was increased to 250.

Table 6 outlines the domain of sampling of the damage parameters during the development of meta-models, prior and after the additional refinement. The parameters related to strength were normalized by the identified value of S_{13}, while the parameters related to toughness were normalized with the value of $G_{Ic-inter}$ identified through the DCB simulations. The parameters related to the fibre law are normalized using the maximum stress peak and the corresponding strain in the tensile test of specimen B1. For the dimensionless parameters, the real values are reported.

5.2. Results of the optimization procedure on the surrogate model

The algorithm reached the maximum number of generations, but Fig. 16 highlights that the procedure reached an appreciable convergence.

The material parameters that achieved the best scores are reported in the last column of Table 6. These values were used to simulate the tensile tests of specimens B1, F3 and H2 by Abaqus/Explicit analyses. The verification pointed out that computing the indicators of maximum force and total area through meta-models instead of directly through Abaqus/Explicit led to an average percentual error of about 4 %, which was

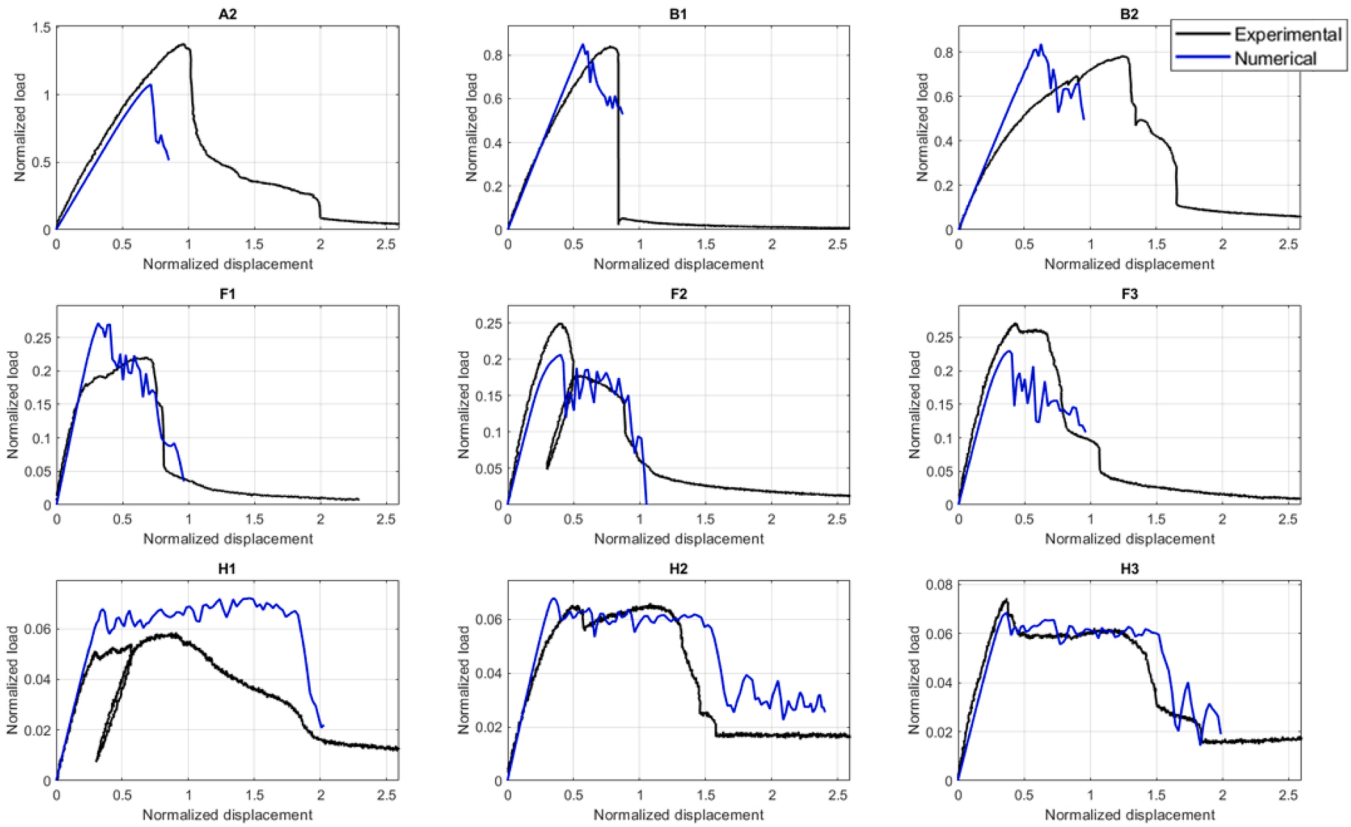

Fig. 17. Numerical correlation of load displacement curves after optimization.

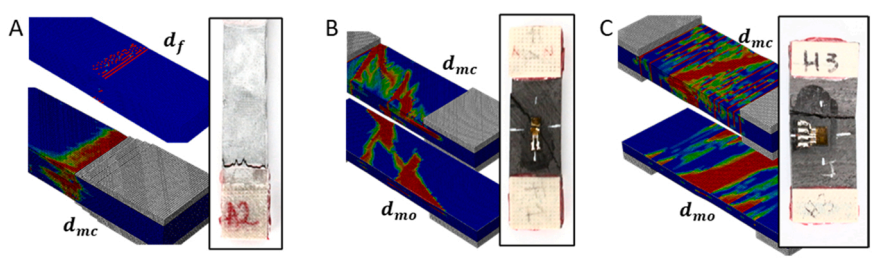

Fig. 18. Numerical failure modes of specimens B1 (A), F3 (B) and H2 (C).

deemed a satisfying performance for the regression model.

Finally, the parameters of Table 6 were adopted to simulate the tensile test of all the nine specimens involved in the tensile test campaign, to assess the quantitative and the qualitative correlation obtained by the modelling technique calibrated through the genetic approach applied to the regression model. Despite the simpleness of the objective function and the complexity of both the lamination sequences and the non-linear responses, the results were particularly interesting. The largest error was the maximum load of Chordal specimen A2, while the peak forces in the other Chordal specimen were captured with good precision. The overall trends in the matrix-dominated responses of Pseudo-45 and Radial specimens were represented with a remarkable degree of correlation. The errors in the peak forces were limited and the shape of the numerical curves, in the post-failure regime, were very similar to the experimental ones. The total energy required for specimen failure was well represented. Overall, the numerical model can adequately represent the load-displacement curves of specimens with different and complex lamination sequence and critically different responses (see Fig. 17). The major issue is apparently related to the difficulty in representing the non-linear behaviour of chordal specimens even if, again, the quantitative correlation in terms of maximum force can be deemed adequate for two specimens out of three.

Further analyses and sensitivity studies were carried out to investigate such aspect of the correlation. Results indicated that a better representation of the non-linearity of Chordal specimens cannot be achieved with the adopted decomposition, unless a non-linear fibre phase is used. Alternatively, a stiffer matrix phase in the fibre direction

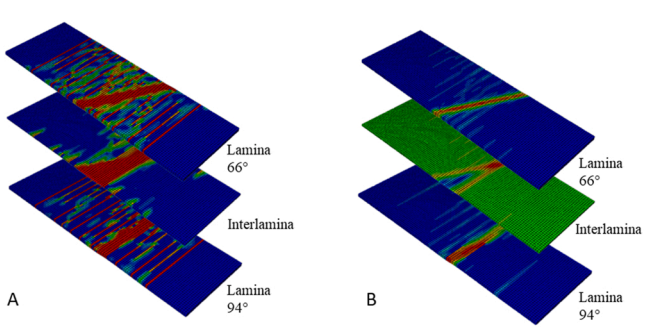

Fig. 19. Contour of matrix damage variables (A) and of the logarithmic strain ε_{11}^{L} (B) in two laminae of specimen H2 and in their interface.

would be necessary. Also, a partial debonding of the tabs, promoted by the damage induced in the tab region, could have contributed to the observed results. However, these considerations regarding the response of the fibre and of the matrix could indicate a role of the mat material that is needled during the manufacturing process, which in the present work was included in the homogenized model of the ply.

A further confirmation of the quality of the results was obtained by the analysis of failure modes, which is exemplified by the contours of the matrix and fibre damage variables shown in Fig. 18 for three specimens. Within the limits constituted by the spread of the fracture development in continuum elements and the regularity of the mesh, quite neat matrix cracks oriented in the same direction of the experimental results can be observed, with a clear dependence on the reinforcement direction.

Overall, it must be remarked that the proposed meso-scale approach achieved a noticeable experimental-numerical correlation, especially for matrix-dominated responses, for laminates subjected to very complex and very different stress states. Considering also the plainness of the objective function adopted during the identification of parameters, the results provide a strong indication that the selected form of matrix damage laws was consistent with the physical behaviour of the material. Indeed, such consistency can explain how the simple search for a matching of maximum force and overall toughness could have led to the appreciable experimental-numerical correlation obtained for the specimens considered in the studies.

The role of delamination and of inter/intralaminar damage coupling deserves additional comments, which can be introduced by considering the strain contour shown in Fig. 19.

If the evolution of intralaminar damage d_{mc} in adjacent plies is analysed, like in Fig. 18 for the radial specimen H2, it can be observed that in each lamina damage evolved perpendicularly to the reinforcement, as expected in physical specimens. However, such outcome requires that a delamination damage d_{mo} is developed between the plies, as indicated in Fig. 18-A. This makes possible the localization of the strain along different fracture lines, as presented in Fig. 18-B. Accordingly, the coupling parameter h, identified at a value of 0.63 by the optimization process, is likely to have played a significant role in the final failure process and particularly in determining the displacement levels corresponding to the drop of load carrying capability in the specimens, which were appreciably captured by the numerical models for all the Pseudo-45 and Radial specimens, as it can be seen in Fig. 16.

6. Conclusions

The findings of the research activity indicate that the numerical model and the identification strategy proposed in the paper can be considered promising tools to study C/C elements with 2.5D fibre reinforcement architectures, whenever their role requires the analysis of structural integrity. The case of automotive brake discs that motivated the research is a clear, but non exhaustive example.

A first finding of the activity is represented by the results of the tests on multi-directional C/C laminates with preferential orientations. Such tests pointed out that the C/C laminates behave in a complex way depending on the orientation of the fibres and exhibit non-linear responses that provide significant toughness levels, which cannot be ignored for realistic structural integrity predictions.

The unconventional lamination sequences involved a challenge for the identification of the material parameters, even in the elastic range. The direct optimization of Finite Element Models proved that such identification is possible and can be carried out on specimens extracted from the final component, thus eliminating the need of producing specimens with homogenous lay-ups and allowing an identification of the properties directly on the manufactured component, which could be considered more reliable due to the potential influences of thickness, geometries, and lay-ups modifications on the CVI process.

The most important finding of the activity is related to the assessment of the bi-phasic approach based on Cohesive Zone Models for representing the non-linear responses, the toughness of the specimens, and the complex damage scenarios involved in the failure of the laminates. The approach also includes the calibration method adopted for the parameters of the damage laws, which relied on innovative non-parametric Gaussian regressions performed on a database of simulations and a subsequent genetic optimization.

The application of the calibrated CZMs both for intra-ply and inter-ply cracks captured the basic aspects of material damage mechanisms, as proved by the qualitative and quantitative correlations achieved. The adequate representations of the physical damage modes provided by CZMs is also confirmed by the fact that the automatic identification could be accomplished by considering only two simple performance indices, namely the maximum force and the overall toughness, for three specimens out of nine. These two quantitative indices allowed obtaining numerical curves with features such as initial non-linearity, force peaks, plateaus and strain softening regimes that are in appreciable agreement with all the individual experimental responses of the specimens with different individual lay-ups, particularly for matrix-dominated specimens. This validates the calibrated material models and strongly suggest that the structure of the constitutive law adopted allows a really effective representation of the inelastic mechanisms in the material.

Finally, it is worth mentioning that such results were achieved in a computationally efficient way, without requiring the use of zero-thickness elements for the interfaces and the consequent numerical issues mentioned in the introduction. Moreover, the adopted modelling technique made possible the introduction of a coupling between the intra-ply and inter-ply damage, which represents an important novelty of the approach. The coupling is deemed to play a significant role in representing the failure of the plies and the delamination in multi-directional laminates within meso-scale models developed at the ply level.

CRediT authorship contribution statement

Alessandro Airoldi: Conceptualization, Methodology, Supervision, Writing – review & editing. **Edoardo Novembre:** Validation, Formal analysis, Visualization, Writing – original draft. **Chiara Mirani:** Software, Validation, Investigation. **Giacomo Gianotti:** Software. **Raffaello Passoni:** Data curation, Project administration. **Carlo Cantoni:** Resources, Supervision.

Declaration of Competing Interest

The authors declare the following financial interests/personal relationships which may be considered as potential competing interests: Alessandro Airoldi reports financial support was provided by Brembo SpA.

Data availability

The raw and processed data required to reproduce these findings cannot be shared at this time due to legal or ethical reasons.

Acknowledgements

The research presented in this paper has been funded by Brembo SpA.

References

[1] E. Savage, Carbon/carbon Composites, Chapman & Hall, London, 1993, pp. 351–367.
[2] E. Fitzer, L.M. Manocha, Carbon Reinforcements and Carbon/carbon Composites, Springer Science & Business Media, 1998.
[3] X. Xiong, B.Y. Huang, J.H. Li, H.J. Xu, Friction behaviors of carbon/carbon composites with different pyrolytic carbon textures, Carbon 44 (3) (2006) 463–467.

[4] T. Windhorst, G. Blount, Carbon-carbon composites: a summary of recent developments and applications, Mater. Des. 18 (1) (1997) 11–15.
[5] T. Yin, Z. Zhang, X. Li, X. Feng, Z. Feng, Y. Wang, L. He, X. Gong, Modeling ablative behavior and thermal response of carbon/carbon composites, Comput. Mater. Sci. 95 (2014) 35–40.
[6] M. Albano, R.B. Morles, F. Cioeta, M. Marchetti, Coating effects on thermal properties of carbon carbon and carbon silicon carbide composites for space thermal protection systems, Acta Astronaut. 99 (2014) 276–282.
[7] L. Xuefeng, Z. Jie, Q. Kun, Densification rate and mechanical properties of carbon/carbon composites with layer-designed preform, Ceram. Int. 45 (4) (2019) 4167–4175.
[8] F.A. Christin, A global approach to fiber nD architectures and self-sealing matrices: from research to production, Int. J. Appl. Ceram. Technol. 2 (2) (2005) 97–104.
[9] Montaudon, M., Fenot, F., Christin, F., Choury, J.J., Novoltex textures for thermostructural materials, in: Proceedings of the Twenty Seventh Joint Propulsion Conference, 1991.
[10] Ellis, R.Testing of Novoltex 3-D carbon-carbon integral throat and exit cones (ITECs), in: Proceedings of the Twenty Fourth Joint Propulsion Conference, 1988.
[11] J. Binner, M. Porter, B. Baker, J. Zou, V. Venkatachalam, V.R. Diaz, A. D'Angio, P. Ramanujam, T. Zhang, T.S.R.C. Murthy, Selection, processing, properties and applications of ultra-high temperature ceramic matrix composites, UHTCMCs–a review, Int. Mater. Rev. 65 (7) (2020) 389–444.
[12] Y. Xu, P. Zhang, H. Lu, W. Zhang, Hierarchically modeling the elastic properties of 2D needled carbon/carbon composites, Compos. Struct. 133 (2015) 148–156.
[13] L.Z. Xue, K.Z. Li, Y. Jia, J.J. Ren, S.Y. Zhang, Effects of hypervelocity impact on thermal expansion behavior of 2.5 D carbon/carbon composites from 850° C to 2500° C, Compos. Struct. 178 (2017) 210–216.
[14] R.S. Almeida, Y. Li, B. Besser, P. Xiao, W. Zhou, A. Brückner, N. Langhof, K. Tushtev, W. Krenkel, K. Rezwan, Damage analysis of 2.5 DC/C-SiC composites subjected to fatigue loadings, J. Eur. Ceram. Soc. 39 (7) (2019) 2244–2250.
[15] I.L. Stimson, R. Fisher, Design and engineering of carbon brakes, Philos. Trans. R. Soc. Lond. Ser. A Math. Phys. Sci. 294 (1411) (1980) 583–590.
[16] G. Savage, Formula 1 composites engineering, Eng. Fail. Anal. 17 (1) (2010) 92–115.
[17] M.V. Rao, P. Mahajan, R.K. Mittal, Effect of architecture on mechanical properties of carbon/carbon composites, Compos. Struct. 83 (2) (2008) 131–142.
[18] B. Drach, I. Tsukrov, T. Gross, S. Dietrich, K. Weidenmann, R. Piat, T. Böhlke, Numerical modeling of carbon/carbon composites with nanotextured matrix and 3D pores of irregular shapes, Int. J. Solids Struct. 48 (18) (2011) 2447–2457.
[19] J. Yu, C. Zhou, H. Zhang, A micro-image based reconstructed finite element model of needle-punched C/C composite, Compos. Sci. Technol. 153 (2017) 48–61.
[20] A.P. Gillard, G. Couégnat, S. Chupin, G.L. Vignoles, Modeling of the non-linear mechanical and thermomechanical behavior of 3D carbon/carbon composites based on internal interfaces, Carbon 154 (2019) 178–191.
[21] S.S. Tzeng, W.C. Lin, Mechanical behavior of two-dimensional carbon/carbon composites with interfacial carbon layers, Carbon 37 (12) (1999) 2011–2019.
[22] P. Chowdhury, H. Sehitoglu, R. Rateick, Damage tolerance of carbon-carbon composites in aerospace application, Carbon 126 (2018) 382–393.
[23] A. Airoldi, C. Mirani, L. Principito, A bi-phasic modelling approach for interlaminar and intralaminar damage in the matrix of composite laminates, Compos. Struct. 234 (2020), 111747.
[24] E. Haug, A. De Rouvray, Crash response of composite structures. Structural Crashworthiness and Failure, CRC Press, 1993, pp. 237–294.
[25] D. Coutellier, P. Rozycki, Multi-layered multi-material finite element for crashworthiness studies, Compos. Part A Appl. Sci. Manuf. 31 (8) (2000) 841–851.
[26] S. Flores, A.G. Evans, F.W. Zok, M. Genet, B. Cox, D. Marshall, O. Sudre, Q. Yang, Treating matrix nonlinearity in the binary model formulation for 3D ceramic composite structures, Compos. Part A: Appl. Sci. Manuf. 41 (2) (2010) 222–229.
[27] B.N. Cox, W.C. Carter, N.A. Fleck, A binary model of textile composites—I. Formulation, Acta Metall. Et. Mater. 42 (10) (1994) 3463–3479.
[28] J. Xu, B.N. Cox, M.A. McGlockton, W.C. Carter, A binary model of textile composites—II. The elastic regime, Acta Metall. Mater. 43.9 (1995) 3511–3524.
[29] M.R. Wisnom, Modelling discrete failures in composites with interface elements, Compos. Part A Appl. Sci. Manuf. 41 (7) (2010) 795–805.
[30] X. Chao, L. Qi, W. Tian, X. Hou, W. Ma, H. Li, Numerical evaluation of the influence of porosity on bending properties of 2D carbon/carbon composites, Compos. Part B Eng. 136 (2018) 72–80.
[31] H. Qiu, Z. Zhu, M. Wang, F. Wang, Y. Ma, L. Lang, P. Ying, Study on crack dynamic propagation behavior and fracture toughness in rock-mortar interface of concrete, Eng. Fract. Mech. 228 (2020), 106798.
[32] H. Qiu, F. Wang, Z. Zhu, M. Wang, D. Yu, C. Luo, D. Wan, Study on dynamic fracture behaviour and fracture toughness in rock-mortar interface under impact load, Compos. Struct. 271 (2021), 114174.
[33] A. Baldi, A. Airoldi, M. Crespi, P. Iavarone, P. Bettini, Modelling competitive delamination and debonding phenomena in composite T-Joints, Procedia Eng. 10 (2011) 3483–3489.
[34] A. Airoldi, G. Sala, P. Bettini, A. Baldi, An efficient approach for modeling interlaminar damage in composite laminates with explicit finite element codes, J. Reinf. Plast. Compos. 32 (15) (2013) 1075–1091.
[35] Airoldi, A., Baldi, A., Coiro, M., Fanteria, D., Lazzeri, L., Mariani, U., Rigamonti, M., Sala, G., Scapinello, F.Improved methodology for the design of damage tolerant helicopter structures in composite materials, in: Proceedings of the Twenty Seventh Symposium of the International Committe on Aeronautical Fatigue and Structural Integrity, 1, Paragon Israel, 2013.
[36] A. Airoldi, A. Baldi, P. Bettini, G. Sala, Efficient modelling of forces and local strain evolution during delamination of composite laminates, Compos. Part B Eng. 72 (2015) 137–149.
[37] S. Ghiasvand, A. Airoldi, P. Bettini, C. Mirani, Analysis of residual stresses and interface damage propagation in hybrid composite/metallic elements monitored through optical fiber sensors, Aerosp. Sci. Technol. 107373 (2022).
[38] R. de Borst, J.J. Remmers, Computational modelling of delamination, Compos. Sci. Technol. 66 (6) (2006) 713–722.
[39] A. Turon, C.G. Davila, P.P. Camanho, J. Costa, An engineering solution for mesh size effects in the simulation of delamination using cohesive zone models, Eng. Fract. Mech. 74 (10) (2007) 1665–1682.
[40] J. Cunha, S. Cogan, C. Berthod, Application of genetic algorithms for the identification of elastic constants of composite materials from dynamic tests, Int. J. Numer. Methods Eng. 45 (7) (1999) 891–900.
[41] C. Maletta, L. Pagnotta, On the determination of mechanical properties of composite laminates using genetic algorithms, Int. J. Mech. Mater. Des. 1 (2) (2004) 199–211.
[42] Y.L. Kang, X.H. Lin, Q.H. Qin, Inverse/genetic method and its application in identification of mechanical parameters of interface in composite, Compos. Struct. 66 (1–4) (2004) 449–458.
[43] P.A. Muñoz-Rojas, E.L. Cardoso, M. Vaz, Parameter identification of damage models using genetic algorithms, Exp. Mech. 50 (5) (2010) 627–634.
[44] AC09036782, in: Anonymus, (Ed.), Standard Test Method for Mode I Interlaminar Fracture Toughness of Unidirectional Fiber-reinforced Polymer Matrix Composites, ASTM Internat., 2007.
[45] S.R. Choi, R.W. Kowalik, Interlaminar crack growth resistances of various ceramic matrix composites in mode I and mode II loading, J. Eng. Gas. Turbines Power 130 (2008) 3.
[46] Ojard, G., Barnett, T., Dahlen, M., Santhosh, U., Ahmad, J., Miller, R.Mode I interlaminar fracture toughness testing of a ceramic matrix composite, in: Proceedings of the Mechanical Properties and Performance of Engineering Ceramics and Composites V: Ceramic Engineering and Science, 31 (2010), 195–206.
[47] R.S. Kumar, Crack-growth resistance behavior of mode-I delamination in ceramic matrix composites, Acta Mater. 131 (2017) 511–522.
[48] Abaqus, Version. 6.14 Documentation, Dassault Systemes Simulia Corporation, 651.6.2 (2014).
[49] MATLAB, 9.8.0.1323502 (R2020a), The MathWorks Inc., Natick, Massachusetts (2020).
[50] Airoldi, A., Baldi, A., Mostosi, V., Sala, G., A bi-phasic approach to model progressive matrix damage in composites: development and application, in: Proceedings of the Fifteenth European Conference on Composite Materials (ECCM15), ECCM, Venice, Italy, 2012.
[51] P. Maimi, J.A. Mayugo, P.P. Camanho, A three-dimensional damage model for transversely isotropic composite laminates, J. Compos. Mater. 42 (25) (2008) 2717–2745.
[52] C.G. Dávila, C.A. Rose, P.P. Camanho, A procedure for superposing linear cohesive laws to represent multiple damage mechanisms in the fracture of composites, Int. J. Fract. 158 (2) (2009) 211–223.
[53] A. Airoldi, C.G. Dávila, Identification of material parameters for modelling delamination in the presence of fibre bridging, Compos. Struct. 94 (11) (2012) 3240–3249.
[54] P.P. Camanho, C.G. Davila, M.F. De Moura, Numerical simulation of mixed-mode progressive delamination in composite materials, J. Compos. Mater. 37 (16) (2003) 1415–1438.
[55] J.M. Berthelot, Transverse cracking and delamination in cross-ply glass-fiber and carbon-fiber reinforced plastic laminates: static and fatigue loading, Appl. Mech. Rev. 56 (1) (2003) 111–147.
[56] S.R. Hallett, W.G. Jiang, B. Khan, M.R. Wisnom, Modelling the interaction between matrix cracks and delamination damage in scaled quasi-isotropic specimens, Compos. Sci. Technol. 68 (1) (2008) 80–89.
[57] M.R. Wisnom, S.R. Hallett, The role of delamination in strength, failure mechanism and hole size effect in open hole tensile tests on quasi-isotropic laminates, Compos. Part A Appl. Sci. Manuf 40 (4) (2009) 335–342.
[58] E. Abisset, F. Daghia, X.C. Sun, M.R. Wisnom, S.R. Hallett, Interaction of inter-and intralaminar damage in scaled quasi-static indentation tests: part 1–experiments, Compos. Struct. 136 (2016) 712–726.
[59] Matérn, B. Spatial Variation, 36, Springer Science & Business Media, 2013.